Eur. Phys. J. A **3**, 115–128 (1998)

THE EUROPEAN PHYSICAL JOURNAL A

Lifetime study of high-spin states in ^{104,105}In

D. Kast[1], A. Jungclaus[1], K.P. Lieb[1], M. Górska[2,3], G. de Angelis[4], P.G. Bizzeti[5], A. Dewald[6], C. Fahlander[4,a], H. Grawe[2], R. Peusquens[6], M. De Poli[4], H. Tiesler[6]

[1] II. Physikalisches Institut, Universität Göttingen, D-37073 Göttingen, Germany
[2] Gesellschaft für Schwerionenforschung, D-64291 Darmstadt, Germany
[3] Institute of Experimental Physics, University of Warsaw, Warsaw, Poland.
[4] Istituto Nazionale di Fisica Nucleare, Laboratori Nazionali di Legnaro, I-35020 Legnaro (Padova), Italy
[5] Istituto Nazionale di Fisica Nucleare, Sezione di Firenze, I-50125 Firenze, Italy
[6] Institut für Kernphysik, Universität zu Köln, D-50937 Köln, Germany

Received: 30 June 1998
Communicated by D. Schwalm

Abstract. In the neutron deficient isotopes ^{104,105}In lifetimes of high spin states in the range from 0.5 ps to 600 ps have been measured in a coincidence recoil distance Doppler shift (RDDS) experiment. By combining the Doppler shift attenuation (DSA) and RDDS methods at few μm flight distances, the problem of delayed feeding has been avoided and very short lifetimes in the range 0.5 - 0.8 ps have been determined. Shell model calculations with strong restrictions for the neutron orbitals reveal good agreement with experimental level energies and still fair agreement for most measured B(M1) and B(E2) values.

PACS. 21.10.Tg Lifetimes – 21.60.Cs Shell model – 23.20.Lv Gamma transitions and level energies – 27.60.+j $90 \leq A \leq 149$

1 Introduction

During recent years our knowledge on excited states in nuclei close to double-magic ^{100}Sn has been extended considerably. A status report on the spectroscopy in this mass region is given in [1]. The level schemes of several light In isotopes have recently been identified and/or extended [2–6]. Parallel to the experimental progress, the understanding of excited states in the isotopes ^{102,103,104}In has been improved by shell model calculations [5,6]. The overall agreement of the results of these calculations with the experimental level energies and γ-ray branching ratios confirmed the validity of the shell model approach and parametrization of single-particle energies and residual interactions of the nucleons as given in [1]. For ^{104}In some discrepancies between the calculation and the experiment for the negative-parity states were recognized, while for ^{105}In no calculations had been published previously, due to the large size of the matrices to be diagonalized in this nucleus. Shell model calculations in a restricted model space were performed for $^{107-113}$In to study magnetic rotation on a microscopic scale [7] employing the interaction used in [1,5,6,8].

Besides level energies and branching ratios, only little is known about absolute γ-ray transition probabilities between the excited states in this mass region. In each nucleus only two or three lifetimes with quite large errors were determined in previous experiments [9]. In ^{104}In, no lifetimes of excited states are known to us, and in ^{105}In only that of the $17/2^+$ and $19/2^+$ yrast states have been analysed [10].

In order to extend our information on absolute transition probabilities, we performed a recoil distance lifetime measurement using a plunger apparatus [11] and the γ-ray spectrometer GASP [12]. This experiment provided for a large number of lifetimes and lifetime limits which, in turn, allowed us to sensitively test the calculated wavefunctions and hence the configuration space and two-body matrix elements used.

2 Experiment

The experiment was performed using the XTU tandem accelarator of the INFN at Legnaro. A 1.2 mg/cm^2 thick ^{58}Ni foil of 99.9% enrichment was bombarded with a ≈5 particle-nA 205 MeV ^{50}Cr beam. The target was mounted in the Cologne plunger [11] in front of a 12.3 mg/cm^2 thick stretched Au-stopper foil. Data were taken at 12 flight distances between 16 and 7000 μm. The distance offset of 12(2) μm was extrapolated from the inverse capacity signal as a function of the distance for the last 20 μm before electric contact between target and stopper, measured without beam on the target. Each flight distance up

[a] *Present address:* Division of Cosmic and Subatomic Physics, Lund University, Sweden

Table 1. Position of the Ge-detectors relative to the beam

Position	Number of det.	combined to ring at
31.7°	2	} 34.6° = "35°"
36.0°	4	
58.3°	2	} 59.4° = "59°"
60.0°	4	
72.0°	4	72°
90.0°	8	90°
108.0°	4	108°
120.0°	4	} 120.6° = "121°"
121.7°	2	
144.0°	4	} 145.4° = "145°"
148.3°	2	

to 262 μm was controlled and regulated via a piezoelectric feedback system. In addition, data were taken at 200 MeV beam energy after mounting a 0.45 mg/cm^2 thick ^{58}Ni target evaporated on a 50 mg/cm^2 Au foil. In this experiment short lifetimes accessible to a Doppler shift attenuation analysis were searched for.

The γ-radiation was detected in the GASP detector array at close geometry, without the inner BGO-ball. The positions of the 40 Compton-suppressed Ge detectors are given in Table 1. Triple or higher fold coincident γ-events with a maximum of two γ's in the 90° ring were registered on tape. The detectors were energy and efficiency calibrated with ^{133}Ba, ^{152}Eu, and ^{56}Co sources for energies from 70 keV up to 3.9 MeV. The 3p evaporation channel ^{105}In was the strongest reaction channel having about 30 % of the total cross section. The 3p1n channel ^{104}In was still one of the major reaction products, with a relative cross section of about 10 %. The strengths of all the other channels can be compared to [8], where the inverse reaction at nearly the same center-of-mass energy is discussed.

3 Data analysis

For each flight distance and in the DSA measurement, the $\gamma\gamma\gamma$ coincidences and higher-fold events on tape were unfolded to $\gamma\gamma$ doubles and sorted into asymmetric matrices, with one particular ring on each axis. The seven rings of GASP listed in Table 1 correspond to 28 different combinations of rings for $\gamma\gamma$ coincidences, with gates to be set in all 7 rings and spectra to be accumulated in the 35°, 59°, 121° and 145° rings. This resulted in a total of 364 matrices for the complete data set. The matrices containing data from identical rings on both axes were symmetrized in order to achieve the full counting statistics in each gate on one axis.

To determine the recoil velocity v of the residual nuclei the positions of the unshifted and Doppler shifted components of five strong lines in ^{105}In were analyzed in the two most forward and two most backward rings at 35°, 59°, 121°, and 145° relative to the beam. Gates were set on the stopped components of the strong $17/2^+ \rightarrow 13/2^+$ 485 keV and $13/2^+ \rightarrow 9/2^+$ 1342 keV E2-transitions in order to avoid contaminations (see Fig. 1). The result of a linear regression of the positions of the shifted peaks versus γ-ray energy gave $v = 10.25(10)\mu$m/ps or 3.42(3) % of the speed of light.

In the analysis of the decay functions we used three different methods to extract lifetimes of excited states from the stop and flight peak intensities: the conventional RDDS approach as presented in [13] and two versions of the differential decay curve method (DDCM) established by Dewald et al. [14,15]. These different strategies will now be outlined as applied in the present experiment.

3.1 DDCM

In order to deduce a lifetime τ of an excited state via DDCM, a coincidence gate is set on the shifted component of a feeding transition (γ^F_{in}) and the intensities I^S_{out} of the stop peak (γ^S_{out}) and I^F_{out} of the flight peak (γ^F_{out}) of a depopulating transition are analyzed. As shown in [14], the lifetime of the state is then given as:

$$\tau = I^S_{out} \cdot (dI^F_{out}/dt)^{-1} \quad (1)$$

The main advantage of this method is that a certain feeding path is selected so that uncertainties about feeding times and intensities of different feeding branches can be avoided. Furthermore, the deduced lifetimes do not depend on the uncertainty of the absolute distance between target and stopper foils. For using this method one needs well-separated stop and flight peaks for gating on the populating transition and in the "look" spectra as well. Therefore only spectra of the four rings at 35°, 59°, 121°, and 145° are well suited for this method.

Coincidence gates were set on a flight peak in each of these four rings. Each gate gives four "look" spectra at each distance, i.e. $4 \times 4 \times 12 = 192$ spectra for one combination of a populating and a depopulating transition. At each distance the resulting "look" spectra for each ring were summed up to improve the counting statistics. In these summed spectra the intensities of stop and flight peaks were determined. Finally, the intensities I^S_{out} and I^F_{out} were summed over the same four "look" rings. The slopes of I^F_{out} were analyzed by a spline program using third order polynomials to connect the data points [16]. Finally, the lifetime τ was extracted for all distances according to formula (1). The τ-values obtained in the sensitive distance region were weighted according to their errors. When applying this algorithm we rejected all those spectra where either the gate on the populating transition contained unshifted lines coincident with the depopulating transition or where the analyzed peaks in the "look" spectra were contaminated.

A crucial point in the lifetime analysis in a plunger measurement is a reliable normalization of the data taken at different distances. Due to the trigger condition of at least three coincident γ rays, the γ-emission after β-decay and Coulomb excitation was excluded from the recorded data. Therefore it is reasonable to normalize the reaction directly to the number of collected events. To take the

effect of absorption into accounct as carefully as possible, which differs for the individual rings due to geometric asymmetries, we decided to normalize each "look" ring individually. For each of the rings at 35°, 59°, and 121° relative to the beam we determined the sum of all events in those three matrices containing all events of the particular ring in coincidence with those three for all distances. To check the quality of this normalization, we determined the summed intensity I_{check} of stop and flight peaks of three dominant lines in ^{105}In (272, 485, 1342 keV, see figure 1) with gates set on the stop and flight peaks of the two other γ-rays, i.e. six combinations for each distance and each "look" ring. All values of I_{check}, which must be constant, vary by less than two percent. For the 145° ring, where one Ge detector suffered from a threshold walk leading to a systematically higher count rate, the same quality of I_{check} was achieved by taking the normalization of the 121° ring.

3.2 Conventional RDDS

The DDCM as described above was used to determine most of the lifetimes presented in this work. Apart from this, a conventional RDDS analysis was carried out to determine effective lifetimes of weak transitions or lifetimes in cases where flight and stop peak intensities could not be analyzed individually in the spectrum. For that reason gates were set on unshifted components of strong transitions near the ground state in all the rings of GASP, and coincident "look" spectra were accumulated in the rings at 35°, 59°, 121° and 145°. The intensity of a stop peak as a function of the distance, the R(d) function, was derived for each "look" ring, and fitted with analytic functions implementing the proper feeding scenario. If the lifetimes and intensities of feeding transitions are known and the average sidefeeding lifetime can be estimated, the state lifetime can be determined from the R(d) function. The same normalization as described in Sect. 3.1 was used in this analysis.

3.3 Single DDCM

An additional analysis of the R(d) functions discussed in Sect. 3.2 can be done via the singles Doppler decay curve method [17], where the lifetime of a state is given by the intensities of populating (I^S_{in}) and depopulating (I^S_{out}) stop peaks as follows:

$$\tau = -(I^S_{out} - \sum I^S_{in})(dI^S_{out}/dt)^{-1} \qquad (2)$$

This method of analysis has been used in the case of the transitions of 485 keV and 1248 keV in ^{105}In (see Fig. 1).

4 Results

In this section we present the measured lifetimes for ^{105}In and ^{104}In as summarized in Tables 2 and 3. A more detailed discussion is given for the $17/2^+$ and the $27/2^-$ states in ^{105}In. Their values of τ=600(40) ps and τ <0.5 ps mark the full range of lifetimes of all the states investigated. In the first case, a careful treatment of systematic problems resulting from the very long flight path was necessary. In the second case, a Doppler broadened line shape is reported for the first time in a plunger experiment.

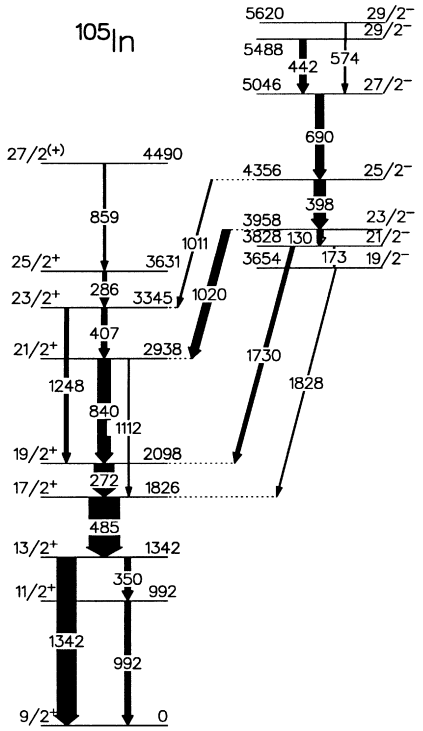

Fig. 1. Relevant part of the level scheme of ^{105}In [6]

4.1 ^{105}In

The relevant part of the level scheme of ^{105}In is shown in figure 1 as recently published by Kownacki et al. [6]. This decay scheme is consistent with our experiment. In particular, the reordering of the 130 and 1730 keV γ-ray transitions as compared to previously published level schemes [4,10] is confirmed by the coincidence of the stopped component of 1730 keV with the shifted component of the 130 keV line. The reverse ordering of the 1730 keV transition above the 130 keV transition would not allow such coincidences. Prior to this work, two lifetimes were published with quite large errors [10], namely 480(150) ps for the $17/2^+$ state and 6(3) ps for the $19/2^+$ state. We confirmed these values with drastically reduced errors and established six new lifetimes and five lifetime limits. Thus we now have lifetime information on the complete yrast cascades above the $17/2^+$ state up to spins of $27/2^{(+)}$ and $29/2^-$. We will discuss first the positive parity states for increasing spins and then the negative parity cascade.

The $11/2^+$ and $13/2^+$ yrast states are depopulated via the M1 transition of 992 keV and the stretched E2 transition of 1342 keV. The lifetimes of these states are too short in comparison to the 485 keV 600 ps feeder transi-

Table 2. Lifetimes of excited states in ^{105}In

E_x [keV]	I^π	$E_{\gamma out}$ [keV]	τ [ps]
1826	$17/2^+$	485	600(40)
2098	$19/2^+$	272	3.76(18)
2938	$21/2^+$	840	0.75(15)
3345	$23/2^+$	1248, 407	2.3(4)
3631	$25/2^+$	286	5.9(2)
4490	$27/2^{(+)}$	859	1.4(3) eff.
3654	$19/2^-$	1828	< 2
3828	$21/2^-$	1730	0.8(1)
3958	$23/2^-$	1020	2.5(2)
4356	$25/2^-$	398	< 2
5046	$27/2^-$	690	< 0.5
5488	$29/2^-_1$	442	1.5(4) eff.
5620	$29/2^-_2$	574	0.9(2) eff.

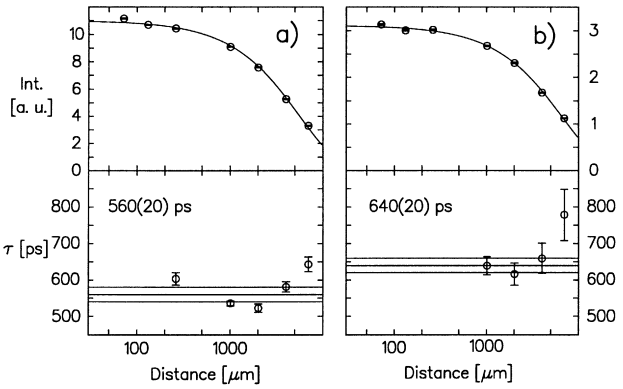

Fig. 2. Analysis of the $17/2^+$ state in ^{105}In. The analysis of the 1342 keV line in the projection of the matrices is shown in **a**. The analysis of the gates below the $17/2^+$ state is given in **b**. For details see text

tion to produce any observable changes in the decay functions of these lines. Although the 485 keV transition is the strongest line observed in the reaction, there were severe difficulties in the determination of the lifetime of the $17/2^+$ state via the analysis described in Sect. 3, due to absorption effects at large flight distances. The Cologne plunger used in connection with the GASP or similar 4π arrays is appropriate for flight distances up to about 1 mm, i.e. lifetimes below about 100 ps at the typical recoil velocity of v = 10 μm/ps. At larger flight distances, the frames of the movable target and fixed stopper foil partially overlap with the sensitive solid angles of individual Ge detectors and may introduce absorption effects which depend on the γ-ray energy and detector position. In the present experiment, only the determination of the 600 ps lifetime of the 1826 keV $17/2^+$ state is directly affected by this problem, both in the decay functions of the 485, 350, 992 and 1342 keV lines, which exhibit this long lifetime, and in the normalization intensities of the rings affected by the shadowing.

For distances of 4 or 7 mm as in our experiment, parts of the flight path were shielded in the different rings of GASP by mechanical parts of the plunger. The γ-radiation from the fixed stopper foil was absorbed to different fractions by the movable target holder in the rings of the backward hemisphere. For that reason, only the γ-radiation from the stopper foil detected in the forward hemisphere was not affected by changes of the distance. Hence, the unshifted components of the 1342 keV and 485 keV lines were analysed in the rings at 35°, 59° and 72°. For this particular case the number of all coincident events in the ring at 35° was used for normalization, because the ring at the extreme forward angle suffered least from the shielding and the efficiency variations with distance. The intensity of the unshifted component of the 1342 keV line was determined directly in the projections of the matrices containing the events in the forward hemisphere. The lifetime was fitted as described in Sect. 3.2 assuming only prompt feeding. This is reasonable because of the fact that the lifetimes of all states above the $17/2^+$ state are shorter by two orders of magnitude. A singles DDCM analysis according to Eq. (2) resulted in τ = 560(20) ps, as shown in Fig. 2a. The other lines below the $17/2^+$ state are not clean enough to determine their lifetimes directly in the projection of the matrices.

In addition, the stop peak intensity of the 1342 keV line was analyzed using the method described in the last paragraph in the sum of gates on the stop peak of the 485 keV line in the forward hemisphere and vice versa, as shown in Fig. 2b. The result of 640(20) ps does not agree with the projection analysis within the individual errors. This is a clear indication to a systematical problem, together with the increase of the values of singles DDCM for the largest distances. This can be either due to an incorrect normalization because of absorbed flight peak intensity, even for the chosen 35°-35° combinations, or to deorientation effects. As we cannot eliminate these uncertainties on the basis of our data alone, our adopted lifetime of the $17/2^+$ state, τ = 600(40) ps, has a larger error than expected statistically. We want to emphasize that these problems are connected to the uncertainty of intensities at distances larger than 1 mm. These uncertainties do not affect any other lifetimes discussed in this work, which are shorter by at least a factor of 10.

The lifetimes of the $19/2^+$, $21/2^+$ and $25/2^+$ yrast states were measured via DDCM. In Fig. 3a, the deduced values of I^S_{out}, $\mathrm{d}I^F_{out}/\mathrm{dt}$ and τ of the 272 keV $19/2^+ \rightarrow 17/2^+$ transition are shown as an example of a lifetime determination with a relative error of only 5%. For the $21/2^+$ state, Fig. 3b shows that the DDCM has its limitations because of the poor statistics of the stop peak intensity which follows from the < 1 ps lifetime of this state. The lifetime values scatter quite strongly, but the adopted value of 0.75(15) ps overlaps with three out of the four points between 28 and 132 μm within their individual errors. The lifetime of the $23/2^+$ state was measured with conventional RDDS because no stop peaks of the depopulating 407 and 1248 keV transitions were observed in the gate on the 286 keV feeding transition. The 1011 keV feeding transition is too weak to set gates on its shifted component. The lifetime of this state has a larger error, due to the unknown sidefeeding time which was estimated to 1.5

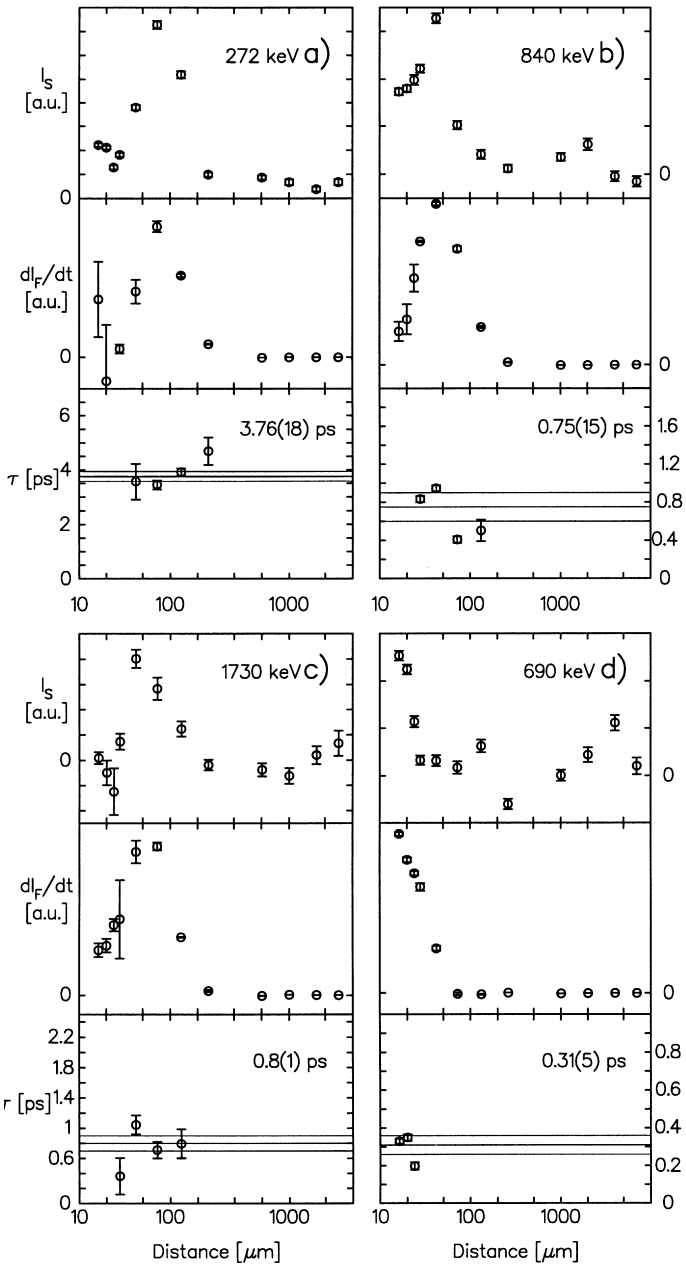

Fig. 3. DDCM analysis in ^{105}In. I_S, dI_F/dt and τ, for the I^{π}=19/2$^+$ (a), 21/2$^+$ (b), 21/2$^-$ (c) and 27/2$^-$ (d) states. The final result for the 27/2 $^-$ state (d)) is $\tau < 0.5$ ps (see text)

(5) ps, with a relative intensity of 40 % of the complete feeding. For the 27/2$^+$ state, only an effective lifetime of 1.4 (3) ps was extracted from the data.

On the negative parity side, the 21/2$^-$ and 23/2$^-$ states were analyzed via DDCM. The data for the 21/2$^-$ state are shown in Fig. 3c. It was possible to set clean gates on the shifted component of the 130 keV feeder only in the rings at 35° and 145°, due to the small Doppler shift at this γ-ray energy. For gating on the shifted component of the 398 keV line we did not use the rings at forward angles because of coincident transitions at 401 and 403 keV in the negative parity cascade of ^{105}In. Likewise, "look" spectra in the ring at 146° were omitted because the flight peak of the 1020 keV line overlapped with the 992 keV stop component. For the 19/2$^-$ and 25/2$^-$ states only upper lifetime limits of 2 ps could be derived.

The 5046 keV 27/2$^-$ state has the shortest lifetime (≈0.3 ps) presented in this work. In the case of instantaneous feeding, the depopulating 690 keV transition would already be completely shifted at the shortest flight distance of 16(2) μm in our experiment. However, due to the delayed population of this state from the 29/2$^-$ states at 5488 keV and 5620 keV having effective lifetimes of 1.5(4) ps and 0.9(2) ps, respectively, the shortest distances of our experiment become sensitive to the lifetime of the 27/2$^-$ state. With the gate on the shifted component of the 442 keV feeder, no stop peak of the 690 keV line was observed. But in the equivalent gate on the shifted component of 574 keV feeder we observed the decay of the 690 keV stop peak between 16 μm to 24 μm, as shown in Fig. 3d. In this case, the feeding time just covers the shortest flight path and thus allowed us to observe the stop peak of the depopulating 690 keV line in coincidence. A DDCM analysis of these data coincident with the 574 keV flight peak results in a lifetime τ=0.31(5) ps for the 27/2$^-$ state. We decided to give only an upper lifetime limit of 0.5 ps as final result for this state because we cannot explain, why one cannot find a stopped component of the depopulating 690 keV transition in coincidence with the shifted component of the 442 keV feeder with four times higher intensity compared to the 574 keV feeder.

The delayed population of the 27/2$^-$ state at the end of the short flight path, indeed, leads to Doppler broadened lineshape of the 690 keV line shown in Fig. 4a. Here, gates were set on the stop peaks at 1342 keV and 485 keV and the "look" spectra were summed up at forward (35°) and backward (145°) angles for the distance of 16 μm. Figure 4b displays the corresponding spectra taken at 35° and 145° with the ^{58}Ni/Au DSA bilayer target. In Fig. 4a Doppler broadened tails of the lineshape representing those nuclei which have survived the 16 μm flight path and decay during the stopping process can indeed be discerned. In contrast, the corresponding DSA spectra taken with the bilayer target shown in Fig. 4b do not exhibit any differences between forward and backward angles because the stopping process is completed before the 27/2$^-$ state decays.

4.2 ^{104}In

Prior to our work no lifetimes of excited states in the nucleus ^{104}In were known. The level scheme was compiled by Johnson et al. [2] and extended by Seweryniak et al. [5]. The part relevant for this work is shown in Fig. 5. This odd-odd nucleus has a very complex decay scheme with a high density of lines which considerably affects the possibility of analyzing plunger data. We were able to determine five lifetimes between 0.6 ps and 38 ps and, in addition, seven upper lifetime limits. We will again discuss our results summarized in Table 3, first for states of positive and then for states of negative parity.

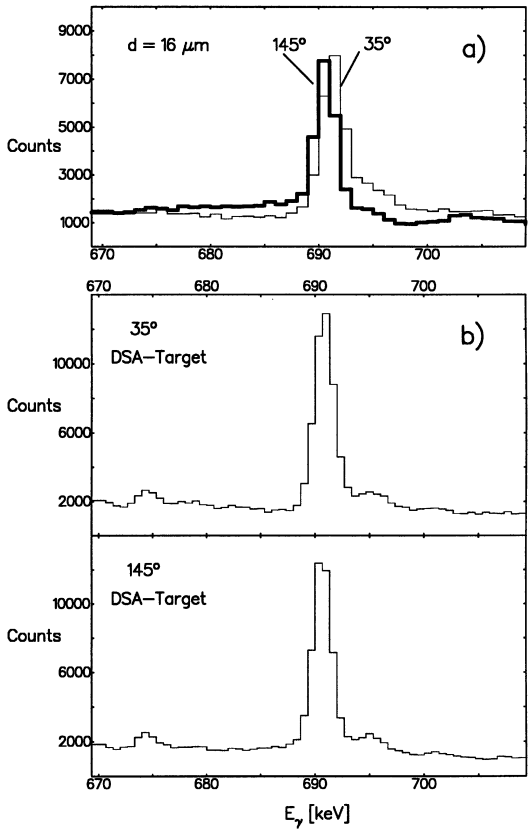

Fig. 4. Lineshape of the 690 keV line depopulating the $27/2^-$ state in ^{105}In. **a** measured with the plunger at a distance of 16 μm, **b** measured with the DSA target

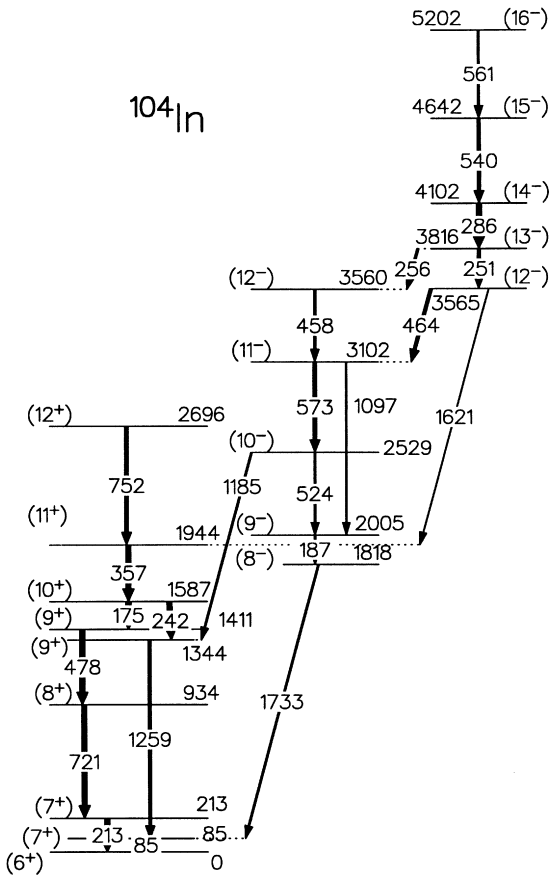

Fig. 5. Relevant part of the level scheme of ^{104}In [5]

Table 3. Lifetimes in ^{104}In

E_x [keV]	I^π	$E_{\gamma out}$	τ [ps]
213	(7_2^+)	213	8.8(5)
1344	(9_1^+)	1259	5(1) eff.
1587	(10_1^+)	175	38(2)
1944	(11_2^+)	357	1.2(4)
2696	(12_1^+)	752	2.3(3) eff.
2529	(10_1^-)	1185	< 5
3102	(11_1^-)	573	< 5
3560	(12_1^-)	458	< 5
3565	(12_2^-)	464	0.57(8)
3816	(13_1^-)	251	< 5
4102	(14_1^-)	286	0.86(7)
4642	(15_1^-)	540	1.0(5) eff.

The 85 keV (7^+) yrast state decays via an 85 keV transition which does not allow any lifetime determination because of its low transition energy. The 213 keV (7_2^+) state has a lifetime of 8.8(5) ps which was analyzed via DDCM by setting a gate on the flight peak of the 721 keV feeder transition (see Fig. 6a). In the cascade of the stretched M1 transitions 478 keV - 175 keV - 357 keV, the 1587 keV (10^+) and 1944 keV (11^+) states were examined via DDCM. The data of the (10^+) state resulting in $\tau = 38(2)$ ps are shown in Fig. 6b. Only in the ring at 35°, the flight and stop peaks of the 175 keV depopulating line were completely separated. Knowing this lifetime, we determined the effective lifetime of the 1344 keV (9^+) yrast state. An analysis of the R(d) function of the 1259 keV line in spectra gated with the subsequent 85 keV transition yielded $\tau_{eff} = 5(1)$ ps for the (9^+) level. The relative error of the 1.2(4) ps lifetime of the 1944 keV (11^+) yrast state is quite large because of the weak stop peak intensity in the spectra. The lifetime of the (8^+) state at 934 keV is too short to observe any depopulating stop peaks in gates on the shifted component of the 478 keV feeder whose effective lifetime is dominated by the relatively slow 175 keV transition above ($\tau = 38(2)$ ps).

On the negative parity side a strong M1 cascade occurs starting at the 1818 keV (8^-) yrast state and extending up to the 6152 keV (18^-) state [5]. This sequence has very irregular energy spacings and a complex feeding pattern. Lifetimes have been determined for the 3560 keV (12^-) yrare state and 4102 keV (14^-) yrast state (see Figs. 6c and 6d). Due to the high density of lines, no other lifetimes of states at negative parity were determined. However, the short effective lifetime of the 9^+ yrast state of 5(1) ps implies $\tau(10_1^-) < 5$ ps and $\tau(13_1^-) < 5$ ps. These are reasonable limits for M1 transitions with energies between 400 and 600 keV as those depopulating the 12^-, 11^- and 10^- states. An additional support for the short lifetime limit $\tau(13_1^-) < 5$ ps comes from the short lifetime of the

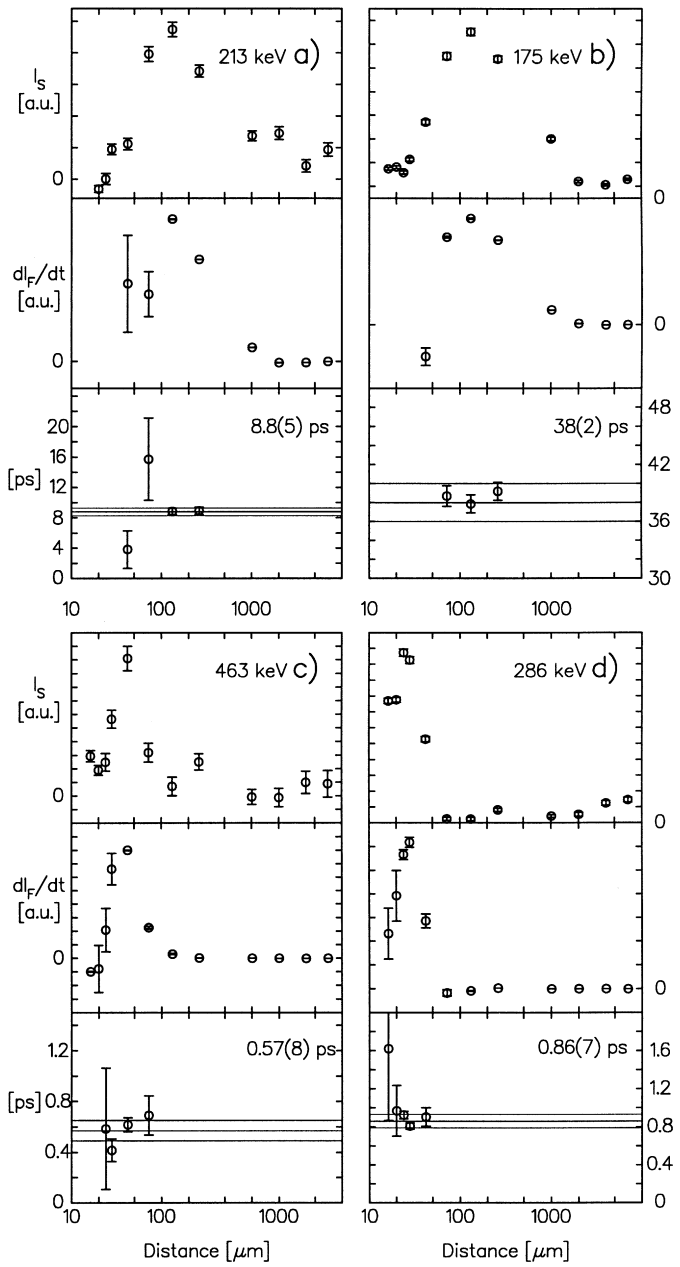

Fig. 6. Data of the DDCM analysis in ^{104}In for the $I^\pi = (7_2^+)$ **a**, (10_1^+) **b**, (12_2^-) **c** and (14_1^-) **d** states

3560 keV (12_2^-) state , τ = 0.57(8) ps , which excludes any long feeding time.

5 Comparison with shell model calculations

5.1 Excitation energies

Isotopes in the neighborhood of the doubly-magic Z=N=50 core ^{100}Sn obviously are ideal candidates for testing the nuclear shell model, and several approaches have been presented to describe the high spin states in this mass region. Levels in the light In isotopes (Z=49, N=53-57) near their ground states are dominated by the proton hole in the $g_{9/2}$ or $p_{1/2}$ orbit and neutron particles in the $d_{5/2}$, $g_{7/2}$, $s_{1/2}$, $d_{3/2}$, and $h_{11/2}$ orbits. To make the calculations feasible, one evidently has to restrict the number of neutrons in the various orbits. Furthermore, when increasing the spin, the number of $h_{11/2}$ neutron particles and $g_{9/2}$ proton holes plays a major role.

Shell model calculations for the light In isotopes $^{102-104}$In and ^{106}In have been carried out by several authors [3–6]. In the work of Seweryniak et al. on ^{102,104}In [5] and Kownacki et al. on ^{103}In [6], up to two neutrons in the $d_{3/2}$ orbit and not more than three neutrons at a time in the $s_{1/2}$, $d_{3/2}$, and $h_{11/2}$ orbits have been considered. Quite good agreement of the calculated energies and γ-ray branching ratios was obtained, but the negative parity states in ^{104}In were predicted $\approx$ 600 keV higher than the measured levels. Shell model calculations for ^{106}In have also been carried out, with at most one neutron in the $h_{11/2}$ orbit, but have been considered unsatisfactory [5]. The first excited states in ^{103}In [3] and ^{105}In [4] have been explained without any $h_{11/2}$ neutrons.

In the present shell model calculations for ^{104}In and ^{105}In, we adopted all the parameters, i.e. single-particle energies, two-body matrix elements and effective single-particle E2 charges and magnetic moments, from the previous attempts [1,5]. A compromise had to be reached between the feasibility of the calculation on one hand and on the other hand the need to include the $h_{11/2}$ neutron orbit to describe the negative parity yrast sequences in the odd In isotopes as demonstrated by the shell model calculation for ^{103}In by Kownacki et al. [6]. Therefore, we allowed for one neutron in this intruder orbit. The basis states in ^{105}In therefore can be written as $[\pi(g_{9/2}$ or $p_{1/2})^{-1} \otimes \nu(g_{7/2}, d_{5/2}, s_{1/2}, d_{3/2})^{6-n}\ \nu(h_{11/2})^n]$ with n=0 or 1, which we abbreviate by π(g or p) $\nu((gd)sd_{3/2}h)$. No proton excitations across the Z=50 gap were taken into account. The calculations were performed with the code RITSSCHIL [18].

Comparisons of the measured and predicted level schemes in ^{105}In and ^{104}In are presented in Figs. 7 and 9, respectively. The yrare states are also included in the figures as far as they are observed experimentally. In ^{105}In, neither energies nor wavefunctions could be calculated for states with $I^\pi < 13/2^+$ and $23/2^-$ because the size of the matrices to be diagonalized was too large, even when applying the restrictions of the model space indicated above. For that reason, the experimental and theoretical $17/2^+$ states were lined up in energy. The mean level deviations (MLD) calculated considering all the states shown in Figs. 7 and 9 are given in Table 4. The very good agreement for the positive parity yrast states in ^{105}In is reflected in the small mean level deviation of only 60 keV. Still acceptable agreement was achieved for the negative parity yrast and yrare states leading to MLD=212 keV (see Fig. 7 and Table 4). Note that the relative spacings of the calculated negative parity yrast states match the experimental values very well, as can be seen in Fig. 8. As one can see from the irregularity of these energy spacings the negative parity yrast cascade

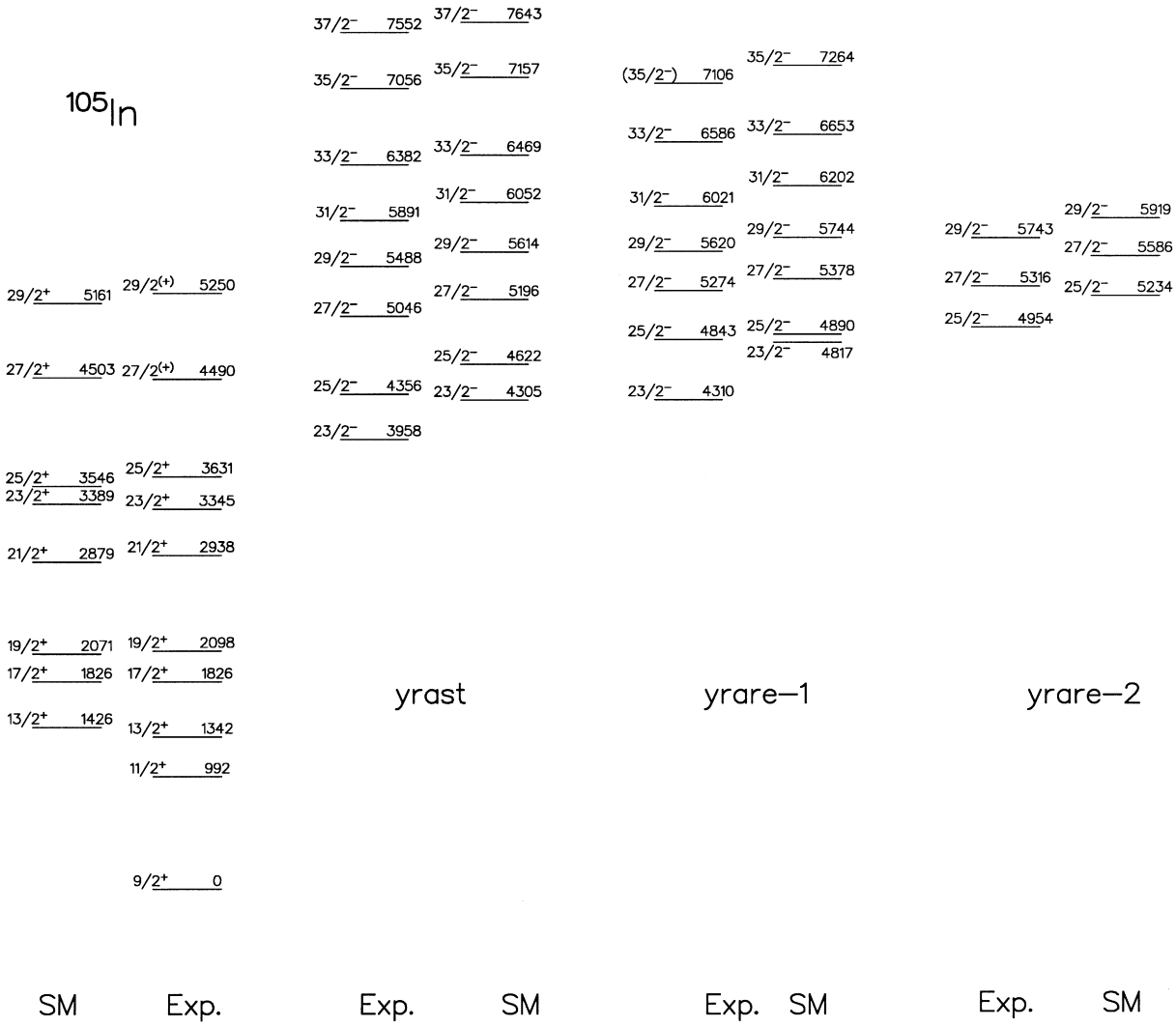

Fig. 7. Experimental and calculated level energies in ^{105}In

in ^{105}In is not typical magnetic rotation as discussed for heavier In-isotopes in [7].

Although in general the wavefunctions in ^{105}In summarized in Table 5 are quite mixed with typically three to five different partitions above 5% for each level, the states at positive parity are dominated by the seniority $v = 3$ configuration $\pi(g_{9/2})^{-1} \otimes \nu(g_{7/2},\, d_{5/2})^2$ up to the highest possible spin $I^\pi = 21/2^+$ of this configuration and $\pi(g_{9/2})^{-1} \otimes \nu(g_{7/2},\, d_{5/2})^4$ ($v = 5$) above. All the calculated negative parity levels except for the $25/2^-_2$ state (compare Table 5) contain a neutron excitation into the $h_{11/2}$ orbit. This is intelligible since deriving the odd parity from a $p_{1/2}$ proton instead, the $23/2^-$ and $25/2^-$ states can only be build with a maximum seniority $v = 7$ configuration. Note, that all the experimental levels up to 7.6 MeV excitation energy are accounted for in the calculation as seen in Fig. 7. The highest observed spins of $29/2^+$ and $37/2^-$ correspond to the maximum spins of the $v = 5$ configurations $\pi(g_{9/2})^{-1} \otimes \nu(gd)^4$ and $\pi(g_{9/2})^{-1} \otimes \nu(gd)^3(h_{11/2})^1$, respectively.

Table 4. Mean level deviations for levels in Figs. 7 and 9 [keV]

	$\pi = +$	$\pi = -$
^{105}In	60	212
^{104}In, 1 $h_{11/2}$	171	108
^{104}In, 3 $h_{11/2}$*	163	501

*: calculated energies taken from [5]

For ^{104}In, we have compared the experimental high spin scheme with both our shell model calculation (SM-1) and the one of [5] (SM-3) where up to three $h_{11/2}$ neutrons were considered. Whereas the positive parity states are equally well described by both approaches, the levels at negative parity are much better reproduced by our calculation as can be seen in Fig. 9. Especially the overall shift of about 600 keV to higher energies in the previous $\nu(h_{11/2})^3$ calculation has disappeared. This improvement

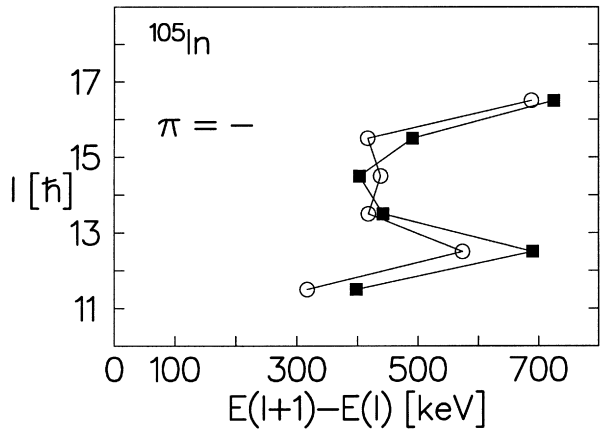

Fig. 8. Experimental (*filled squares*) and calculated (*open circles*) energy spacings between negative parity yrast states in ^{105}In

is measured by the decreased MLD of 108 keV as compared to 501 keV for SM-3. At first sight, one would expect an opposite behaviour, namely a deterioration of the description when restricting the number of neutrons in the $h_{11/2}$ orbit. One possible explanation is that the deficiency of the SM-3 approach arises from an inadequate interaction within the $h_{11/2}$ neutrons, which is switched off in SM-1. Note, that the interaction involving the $h_{11/2}$ orbit has been derived from the lead region using a (208/A) scaling instead of a more appropriate $(208/A)^{1/3}$ scaling (see [1] and refs. therein). A second possible explanation is given by the authors of [5] who interpret this energy shift as indication that the proton-neutron two-body matrix elements involving the $h_{11/2}$ neutron orbital do not reproduce the correct $h_{11/2}$ single-particle energy, when moving into the proton shell. This is supported by the observation that the $h_{11/2}$ states are well reproduced in the tin isotopes [1]. We would like to point out that besides the excitation energies both calculations also differ considerably concerning the structure of the negative parity states. Whereas in the present calculation the dominant configurations (80-90%) of the 8^-, 9^-, 10^-, and 11^- yrast and the 12^- yrare states contain a $p_{1/2}$ proton hole and no neutron in the $h_{11/2}$ intruder orbit, all negative parity levels in SM-3 involve a $h_{11/2}$ neutron and a $g_{9/2}$ proton hole.

5.2 Transition strengths in ^{105}In

In general, the agreement between experimental and calculated transition strengths is rather good in ^{105}In as can be seen from Table 8 and Fig. 10a. When comparing experimental and theoretical transition strengths, we assumed pure dipole character for all ΔI=1 transitions and therefore we set the unknown mixing ratios δ=0. Internal conversion coefficients according to [19] were taken into account. As in many nuclei of this mass region, strong stretched M1 transitions of the order of 0.2-1.5 W.u. and E2 transitions of a few W.u. are both observed and calculated. The small E2 strengths confirm the sphericity of

Table 5. Calculated wavefunctions in ^{105}In. The partitions are explained in the text. The notation $\nu(g^2d^4)^2_4$ means that the 4 neutrons in the $d_{5/2}$ orbit and the 2 neutrons in the $g_{7/2}$ orbit have seniority $v_\nu = 2$ and couple to spin 4

I^π	partition	fraction [%]
$13/2^+$	$\pi g\nu(g^2d^4)^2_2$	26.3
	$\pi g\nu(g^2d^4)^2_4$	16.5
$17/2^+$	$\pi g\nu(g^1d^5)^2_5$	21.4
	$\pi g\nu(g^1d^5)^2_4$	11.1
	$\pi g\nu(g^2d^4)^2_4$	10.1
	$\pi g\nu(g^2d^4)^2_6$	6.0
$19/2^+$	$\pi g\nu(g^1d^5)^2_6$	29.9
	$\pi g\nu(g^1d^5)^2_5$	21.7
	$\pi g\nu(g^3d^3)^2_6$	9.0
	$\pi g\nu(g^3d^3)^2_5$	4.7
$21/2^+$	$\pi g\nu(g^2d^4)^2_6$	37.4
	$\pi g\nu(g^2d^4)^4_8$	21.0
$23/2^+$	$\pi g\nu(g^2d^4)^4_9$	17.2
	$\pi g\nu(g^2d^4)^4_7$	14.6
	$\pi g\nu(g^2d^4)^4_8$	12.8
	$\pi g\nu(g^3d^3)^4_8$	10.0
	$\pi g\nu(g^3d^3)^4_{10}$	5.9
	$\pi g\nu(g^3d^3)^4_7$	5.8
$25/2^+$	$\pi g\nu(g^2d^4)^4_8$	36.7
	$\pi g\nu(g^2d^4)^4_{10}$	26.7
	$\pi g\nu(g^2d^4)^4_9$	16.9
$27/2^+$	$\pi g\nu(g^2d^4)^4_{10}$	53.0
	$\pi g\nu(g^2d^4)^4_9$	20.9
$23/2^-_1$	$\pi g[\nu(g^1d^4)^1_{7/2}h]_9$	38.8
	$\pi g[\nu(g^3d^2)^1_{7/2}h]_9$	7.3
	$\pi g[\nu(g^1d^4)^3_{11/2}h]_{11}$	6.5
	$\pi g[\nu(g^1d^2)^1_{7/2}(d^2_{3/2})_0h]_9$	5.5
$23/2^-_2$	$\pi g[\nu(g^2d^3)^1_{5/2}h]_8$	20.3
	$\pi g[\nu(g^2d^3)^1_{5/2}h]_7$	10.1
	$\pi g[\nu(d^5)^1_{5/2}h]_8$	6.5
	$\pi g[\nu(d^5)^1_{5/2}h]_7$	5.7
$25/2^-_1$	$\pi g[\nu(g^1d^4)^1_{7/2}h]_9$	36.7
	$\pi g[\nu(g^1d^4)^3_{11/2}h]_{11}$	11.4
	$\pi g[\nu(g^3d^2)^1_{7/2}h]_9$	7.3
	$\pi g[\nu(g^1d^2)^1_{7/2}(d^2_{3/2})_0h]_9$	5.0
$25/2^-_2$	$\pi p\nu(g^3d^3)^6_{12}$	84.5
$25/2^-_3$	$\pi g[\nu(g^1d^4)^3_{11/2}h]_{11}$	12.6
	$\pi g[\nu(g^1d^4)^3_{11/2}h]_{10}$	9.1
	$\pi g[\nu(g^1d^4)^3_{9/2}h]_{10}$	5.4
$27/2^-_1$	$\pi g[\nu(g^1d^4)^3_{11/2}h]_{11}$	38.7
	$\pi g[\nu(g^1d^4)^1_{7/2}h]_9$	7.8
	$\pi g[\nu(g^1d^3)^2_5sh]_{11}$	6.2
$27/2^-_2$	$\pi g[\nu(g^1d^4)^3_{11/2}h]_{10}$	9.7
	$\pi g[\nu(g^1d^4)^3_{9/2}h]_{10}$	7.0
	$\pi g[\nu(g^2d^3)^3_{15/2}h]_{13}$	6.6
	$\pi g[\nu(g^2d^3)^3_{11/2}h]_{11}$	6.4
$27/2^-_3$	$\pi g[\nu(g^2d^3)^3_{9/2}h]_{10}$	9.3
	$\pi g[\nu(g^2d^3)^3_{13/2}h]_{12}$	7.4
	$\pi g[\nu(g^2d^3)^3_{11/2}h]_{11}$	6.7
$29/2^-_1$	$\pi g[\nu(g^1d^4)^3_{11/2}h]_{11}$	22.2
	$\pi g[\nu(g^2d^3)^3_{15/2}h]_{13}$	14.0
	$\pi g[\nu(g^2d^3)^3_{11/2}h]_{11}$	6.4
$29/2^-_2$	$\pi g[\nu(g^1d^4)^3_{11/2}h]_{11}$	27.3

Table 5. Continued

I^π	partition	fraction [%]
$29/2^-_3$	$\pi g[\nu(g^2d^3)^3_{15/2}h]_{13}$	14.3
	$\pi g[\nu(g^1d^4)^3_{13/2}h]_{11}$	8.6
	$\pi g[\nu(g^1d^4)^3_{11/2}h]_{11}$	7.4
	$\pi g[\nu(g^1d^4)^3_{11/2}h]_{10}$	5.6
	$\pi g[\nu(g^2d^3)^3_{11/2}h]_{11}$	5.0

Table 6. Calculated wavefunctions of positive parity states in ^{104}In. The partitions are explained in the text. The notation is the same as in table 5

I^π	partition	fraction [%]
6^+_1	$\pi g\nu(g^1d^4)^1_{7/2}$	23.5
	$\pi g\nu(g^2d^3)^1_{5/2}$	15.0
	$\pi g\nu(g^2d^3)^3_{3/2}$	9.0
7^+_1	$\pi g\nu(g^1d^4)^1_{7/2}$	24.1
	$\pi g\nu(d^5)^1_{5/2}$	17.1
	$\pi g\nu(g^2d^3)^1_{5/2}$	10.4
	$\pi g\nu(g^3d^2)^1_{7/2}$	6.8
	$\pi g\nu(g^1d^4)^3_{11/2}$	6.5
7^+_2	$\pi g\nu(g^2d^3)^1_{5/2}$	22.9
	$\pi g\nu(g^1d^4)^1_{7/2}$	19.3
	$\pi g\nu(d^5)^1_{5/2}$	15.1
8^+_1	$\pi g\nu(g^1d^4)^3_{11/2}$	38.9
	$\pi g\nu(g^1d^4)^1_{7/2}$	11.9
	$\pi g[\nu(g^1d^3)^2_5s]_{11/2}$	6.3
8^+_2	$\pi g\nu(g^2d^3)^3_{7/2}$	24.9
	$\pi g\nu(g^2d^3)^3_{9/2}$	22.3
	$\pi g\nu(g^2d^3)^3_{13/2}$	9.2
9^+_1	$\pi g\nu(g^1d^4)^3_{11/2}$	51.7
	$\pi g[\nu(g^1d^3)^2_5s]_{11/2}$	6.6
	$\pi g\nu(g^1d^4)^3_{15/2}$	5.5
9^+_2	$\pi g\nu(g^2d^3)^3_{9/2}$	32.6
	$\pi g\nu(g^2d^3)^3_{13/2}$	16.0
	$\pi g\nu(g^2d^3)^3_{11/2}$	9.8
9^+_3	$\pi g\nu(g^2d^3)^3_{9/2}$	18.8
	$\pi g\nu(g^1d^4)^3_{11/2}$	14.6
	$\pi g\nu(g^1d^4)^3_{9/2}$	12.9
	$\pi g[\nu(d^4)^2_4d_{3/2}]_{11/2}$	5.8
10^+_1	$\pi g\nu(g^1d^4)^3_{13/2}$	20.2
	$\pi g\nu(g^1d^4)^3_{11/2}$	18.2
	$\pi g\nu(g^2d^3)^3_{17/2}$	12.6
	$\pi g\nu(g^2d^3)^3_{13/2}$	9.5
	$\pi g\nu(g^2d^3)^3_{11/2}$	8.7
10^+_2	$\pi g\nu(g^1d^4)^3_{15/2}$	42.3
	$\pi g\nu(g^1d^4)^3_{11/2}$	17.3
	$\pi g\nu(g^2d^3)^3_{15/2}$	6.6
10^+_3	$\pi g\nu(g^2d^3)^3_{15/2}$	14.5
	$\pi g\nu(g^2d^3)^3_{17/2}$	13.8
	$\pi g\nu(g^2d^3)^3_{13/2}$	12.8
	$\pi g\nu(g^1d^4)^3_{11/2}$	10.7
	$\pi g\nu(g^1d^4)^3_{13/2}$	9.2
	$\pi g\nu(g^2d^3)^3_{11/2}$	5.2

Table 6. Continued

I^π	partition	fraction [%]
11^+_1	$\pi g\nu(g^1d^4)^3_{15/2}$	43.8
	$\pi g\nu(g^1d^4)^3_{13/2}$	22.6
	$\pi g\nu(g^2d^3)^3_{17/2}$	7.2
11^+_2	$\pi g\nu(g^2d^3)^3_{17/2}$	31.4
	$\pi g\nu(g^2d^3)^3_{13/2}$	26.7
	$\pi g\nu(g^2d^3)^3_{15/2}$	9.7
11^+_3	$\pi g\nu(g^2d^3)^3_{13/2}$	22.9
	$\pi g\nu(g^2d^3)^3_{15/2}$	15.9
	$\pi g\nu(g^3d^2)^3_{15/2}$	11.0
	$\pi g\nu(g^3d^2)^5_{19/2}$	8.0
	$\pi g\nu(g^2d^3)^3_{17/2}$	7.1
	$\pi g\nu(g^2d^3)^5_{19/2}$	5.1
12^+_1	$\pi g\nu(g^2d^3)^3_{17/2}$	38.6
	$\pi g\nu(g^2d^3)^5_{21/2}$	35.0
12^+_2	$\pi g\nu(g^1d^4)^3_{15/2}$	61.1
	$\pi g\nu(g^3d^2)^3_{15/2}$	7.5
	$\pi g\nu(g^2d^3)^3_{17/2}$	5.3

Table 7. Calculated wavefunctions of negative parity states in ^{104}In. The partitions are explained in the text. The notation is the same as in table 5

I^π	partition	fraction [%]
8^-_1	$\pi p\nu(g^1d^4)^3_{15/2}$	27.4
	$\pi p\nu(g^3d^2)^3_{15/2}$	26.1
	$\pi p\nu(g^2d^3)^3_{17/2}$	24.5
9^-_1	$\pi p\nu(g^2d^3)^3_{17/2}$	76.8
	$\pi p\nu(g^4d^1)^3_{17/2}$	5.4
10^-_1	$\pi p\nu(g^2d^3)^5_{21/2}$	73.5
	$\pi p\nu(g^2d^3)^5_{19/2}$	7.3
	$\pi p\nu(g^3d^2)^5_{19/2}$	6.7
11^-_1	$\pi p\nu(g^2d^3)^5_{21/2}$	80.3
	$\pi p[\nu(g^2d^2)^4_{10}d_{3/2}]_{21/2}$	5.1
12^-_1	$\pi g[\nu(g^1d^3)^2_5h]_{21/2}$	16.8
	$\pi g[\nu(g^1d^3)^2_3h]_{17/2}$	13.4
	$\pi g[\nu(g^1d^3)^2_4h]_{17/2}$	8.2
	$\pi g[\nu(g^1d^3)^2_6h]_{21/2}$	7.5
12^-_2	$\pi p\nu(g^3d^2)^5_{23/2}$	88.5
	$\pi p[\nu(g^3d^1)^4_{10}d_{3/2}]_{23/2}$	5.5
12^-_3	$\pi g\nu(g^1d^3)^2_4h]_{19/2}$	18.3
	$\pi g\nu(g^1d^3)^2_6h]_{23/2}$	9.9
	$\pi g\nu(g^1d^3)^2_5h]_{19/2}$	9.3
	$\pi g\nu(g^1d^3)^5_5h]_{21/2}$	7.1
13^-_1	$\pi g[\nu(g^1d^3)^2_5h]_{21/2}$	31.1
	$\pi g[\nu(g^1d^3)^2_6h]_{21/2}$	11.3
	$\pi g[\nu(g^1d^3)^2_4h]_{19/2}$	5.9
	$\pi g[\nu(g^1d^3)^2_6h]_{23/2}$	5.8
13^-_2	$\pi g[\nu(g^1d^3)^2_6h]_{23/2}$	17.3
	$\pi g[\nu(g^1d^3)^2_4h]_{19/2}$	12.8
	$\pi g[\nu(g^1d^3)^2_5h]_{21/2}$	8.2
	$\pi g[\nu(g^1d^3)^2_6h]_{21/2}$	7.1

Table 7. Continued

I^π	partition	fraction [%]
13^-_3	$\pi g[\nu(g^2d^2)^2_6 h]_{23/2}$	25.5
	$\pi g[\nu(g^1d^3)^2_6 h]_{23/2}$	11.3
	$\pi g[\nu(g^1d^3)^2_5 h]_{19/2}$	8.3
	$\pi g[\nu(g^2d^2)^2_4 h]_{19/2}$	6.4
	$\pi g[\nu(g^1d^3)^2_4 h]_{23/2}$	5.8
14^-_1	$\pi g[\nu(g^1d^3)^2_6 h]_{23/2}$	26.7
	$\pi g[\nu(g^1d^3)^2_5 h]_{21/2}$	26.2
14^-_2	$\pi g[\nu(g^1d^3)^2_6 h]_{23/2}$	21.3
	$\pi g[\nu(g^1d^3)^2_6 h]_{21/2}$	14.3
	$\pi g[\nu(g^1d^3)^2_5 h]_{21/2}$	13.8
	$\pi g[\nu(g^1d^3)^2_4 h]_{19/2}$	5.3
14^-_3	$\pi g[\nu(g^2d^2)^2_6 h]_{23/2}$	41.3
	$\pi g[\nu(g^2d^2)^2_4 h]_{19/2}$	9.1
15^-_1	$\pi g[\nu(g^1d^3)^2_6 h]_{23/2}$	53.5
	$\pi g[\nu(g^1d^3)^2_5 h]_{21/2}$	9.7
	$\pi g[\nu(g^3d^1)^2_6 h]_{23/2}$	5.1
16^-_1	$\pi g[\nu(g^1d^3)^4_8 h]_{27/2}$	19.0
	$\pi g[\nu(g^2d^2)^4_8 h]_{27/2}$	18.2
	$\pi g[\nu(g^2d^2)^4_{10} h]_{31/2}$	12.8
	$\pi g[\nu(g^1d^3)^4_7 h]_{25/2}$	10.5
17^-_1	$\pi g[\nu(g^1d^3)^4_8 h]_{27/2}$	31.1
	$\pi g[\nu(g^2d^2)^4_{10} h]_{31/2}$	27.8
	$\pi g[\nu(g^2d^2)^4_8 h]_{27/2}$	12.8
	$\pi g[\nu(g^1d^3)^4_7 h]_{25/2}$	6.7

the ^{100}Sn core and the need to place the valence neutrons in several single-particle orbits. Taking into consideration that there is only one $g_{9/2}$ proton hole in ^{105}In, strong M1 transitions are only possible if either the neutron partition is identical in the initial and final states and couples with the proton hole to total spins differing by 1 $\hbar$ or the spin of the neutron part of the wavefunction differs by 1 $\hbar$ while the angle between the neutron and the proton spin stays constant. For example, the strong $19/2^+ \rightarrow 17/2^+$ M1 transition connects states with the main partitions $\pi(g_{9/2})^{-1} \otimes \nu(g^1_{7/2}, d^5_{5/2})^2_{I_\nu}$ with $\Delta I_\nu = 1$. The only severe failures of the shell model calculation concern the decay of the $21/2^+$ state and the $27/2^- \rightarrow 25/2^-_2$ M1 transition. In the first case, the $21/2^+ \rightarrow 19/2^+$ M1 transition is predicted to have a strength of only 1.5 mW.u., following from the fact that none of the large components of the two states is connected by an allowed M1 transition but require a forbidden $g_{7/2} \rightarrow d_{5/2}$ single-particle transition. However, the experimental result is B(M1) = 67(13) mW.u.. Also the strength of the second decay branch out of the $21/2^+$ state, namely the $21/2^+ \rightarrow 17/2^+$ E2 transition, is not at all reproduced. It is predicted to be very small by the calculation ($\sim 10^{-3}$ W.u.), in contrast to the measured value of 1.3(4) W.u.. The admixture of the $\pi(g) \otimes \nu(g^1\ d^5)$ partition, which allows the decay into the leading fractions of the $17/2^+$ and $19/2^+$ yrast states, must be higher than predicted. In the calculation, only the $21/2^+_3$ state 254 keV above the yrast state has a partition of 35% of this structure. The $27/2^-_1 \rightarrow 25/2^-_2$ transition, involving a proton $g_{9/2} \rightarrow p_{1/2}$ decay and a change in the neutron configuration $\nu(gd)^3h \rightarrow \nu(gd)^6$, is strictly forbidden in the calculation and has therefore a very small predicted strength of 0.2 mW.u.. This value is smaller by a factor of 350 as compared to our experimental result. The most probable explanation is that the calculated $25/2^-_2$ and $25/2^-_3$ states are interchanged, especially since the former level is the only one in the calculation containing a $p_{1/2}$ proton hole and having seniority $v = 7$.

Table 8. B(M1), B(E2) and B(E1) values in ^{105}In

I^π_i	I^π_f	E_γ [keV]	b exp.	B(M1) [mW.u.] exp.	calc.
$19/2^+_1$	$17/2^+_1$	272	1	410(20)	223
$21/2^+_1$	$19/2^+_1$	840	0.94(1)	67(13)	1.5
$23/2^+_1$	$21/2^+_1$	407	0.59(2)	120(30)	68
$25/2^+_1$	$23/2^+_1$	286	1	223(8)	108
$27/2^+_1$	$25/2^+_1$	859	1	>35	336
$21/2^-_1$	$19/2^-_1$	173	0.09(1)	600(200)	-
$23/2^-_1$	$21/2^-_1$	130	0.16(1)	1200(200)	-
$25/2^-_1$	$23/2^-_1$	398	0.88(1)	>220	1414
$27/2^-_1$	$25/2^-_1$	690	0.95(1)	>180	940
$27/2^-_1$	$25/2^-_2$	203	0.012(2)	>70	0.2
$29/2^-_1$	$27/2^-_1$	442	0.76(4)	> 180	665
$29/2^-_1$	$27/2^-_2$	214	0.12(1)	> 190	483
$29/2^-_2$	$27/2^-_1$	574	0.66(3)	> 100	701
$29/2^-_2$	$27/2^-_2$	346	0.11(2)	> 75	227
				B(E2) [W.u.]	
$17/2^+$	$13/2^+$	485	1	1.72(11)	1.45
$21/2^+$	$17/2^+$	1112	0.06(1)	1.3(4)	$8 \cdot 10^{-4}$
$23/2^+$	$19/2^+$	1248	0.41(2)	1.6(4)	0.79
$27/2^-$	$23/2^-$	1088	0.04(1)	> 1.1	10.4
$29/2^-_1$	$25/2^-$	1132	0.07(1)	> 0.54	4.3
$29/2^-_2$	$25/2^-$	1264	0.15(1)	> 1.1	5.7
				B(E1) [W.u.] exp.	
$19/2^-_1$	$17/2^+_1$	1828	0.91(4)	$> 3.3 \cdot 10^{-5}$	
$19/2^-_1$	$19/2^+_1$	1556	0.09(3)	$> 5.2 \cdot 10^{-6}$	
$21/2^-_1$	$19/2^+_1$	1730	0.91(1)	$9.6(13) \cdot 10^{-5}$	
$23/2^-_1$	$21/2^+_1$	1020	0.71(1)	$1.2(1) \cdot 10^{-4}$	
$23/2^-_1$	$23/2^+_1$	613	0.03(1)	$2.3(8) \cdot 10^{-5}$	
$25/2^-_1$	$23/2^+_1$	1011	0.12(1)	$> 2.5 \cdot 10^{-5}$	
$29/2^-_1$	$27/2^{(+)}_1$	998	0.06(1)	$> 1.3 \cdot 10^{-5}$	
$29/2^-_2$	$27/2^{(+)}_1$	1130	0.09(1)	$> 2.5 \cdot 10^{-5}$	

5.3 Transition strengths in ^{104}In

The experimental and calculated E2 and M1 strengths in ^{104}In are summarized in Table 9 and Fig. 10b. In this odd-odd nucleus, the calculation does not match the experimental data as well as in the case of ^{105}In. Out of the six measured M1 rates, four are reproduced within a factor of 4. The strengths of the $10^+_1 \rightarrow 9^+_2$ and $12^-_2 \rightarrow 11^-_1$ transitions, however, are underestimated by up to two orders of magnitude. Five B(M1) values are in agreement with the experimental lower limits, whereas in five other

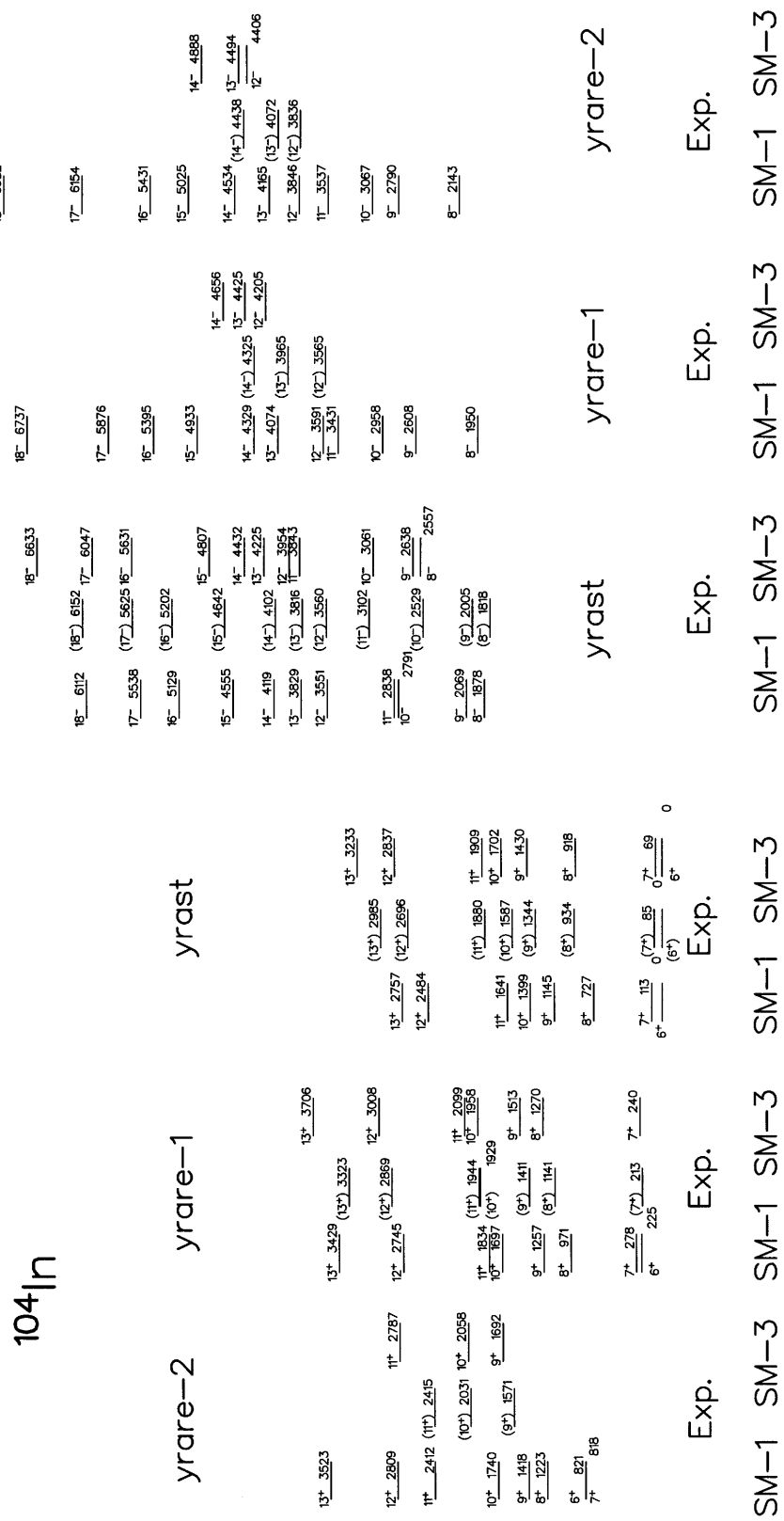

Fig. 9. Experimental and calculated level energies in ^{104}In

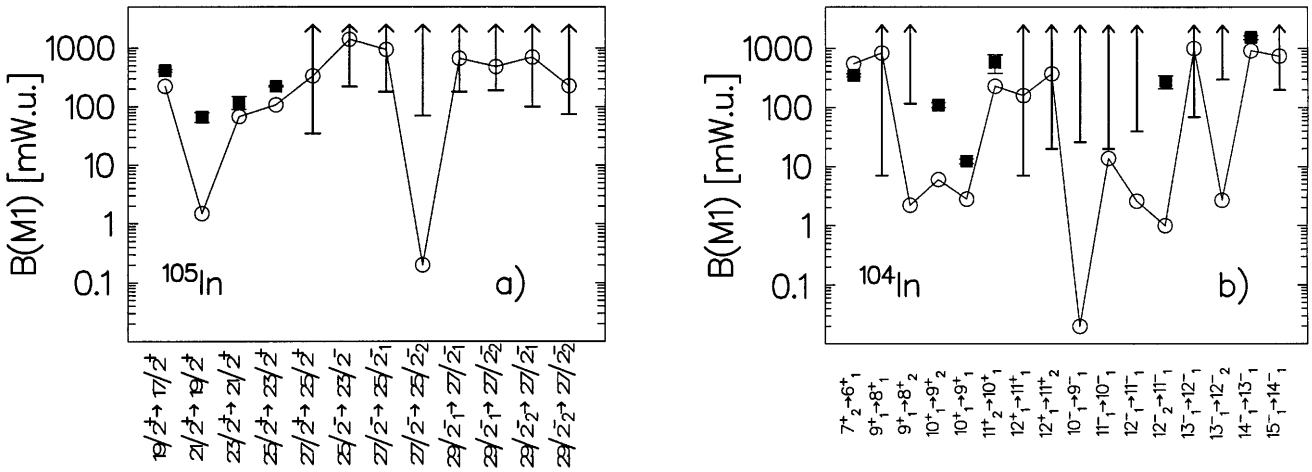

Fig. 10. Experimental (arrows and filled squares) and calculated (open circles) ΔI=1 B(M1) values in ^{105}In (a) and ^{104}In (b)

cases the lower limits already exceed the calculated values by up to two ($13^-_1 \rightarrow 12^-_2$, $12^-_2 \rightarrow 11^-_1$) or in the worst case by even three orders of magnitude ($10^-_1 \rightarrow 9^-_1$). For the E2 transitions shown in Table 9 the agreement is reasonable. Only in the case of the $12^-_1 \rightarrow 10^-_1$ transition the experimental lower limit and the calculated value differ by a factor of 1000.

Looking at Fig. 10b, it seems that the failure of the shell model calculation is most dramatic for all the transitions involving negative parity states with I $\leq 12^-$. This is exactly the spin range where states can be built both based on a $p_{1/2}$ proton hole or a $h_{11/2}$ neutron particle. As mentioned above, the yrast states up to $I = 11^-$ are predicted to contain a $p_{1/2}$ proton hole in our calculation, in contrast to the previous study, where the negative parity states were assigned the structure $\pi(g_{9/2})^{-1} \otimes \nu(h_{11/2})^{-1}$ coupled to the 0^+, 2^+, and 4^+ states in ^{104}Sn [5] leading to different expectations concerning the transition strengths. As already discussed in [6], the interaction used in the present shell model approach seems to overbind the $\pi(p_{1/2})$ hole state. Taking into consideration the comparisons of both the excitation energies and the transition strengths, we have to conclude that the structure of the low-spin negative parity states is not yet well understood.

6 Conclusions

In this work we have determined, via a coincidence recoil distance Doppler shift experiment, lifetimes for the yrast states up to spins $27/2^+$ and $29/2^-$ in ^{105}In and for more than ten states up to (12^+) and (15^-) in ^{104}In. In the analysis, the DDCM and conventional decay curve method have been employed. For the short-lived $27/2^-$ state, the effect of the delayed population on the lineshape in a recoil experiment was observed and could be explained in agreement with the measured lifetimes.

For the first time, shell model calculations for ^{105}In are presented. The restriction of the neutron configura-

Table 9. B(M1) and B(E2) values in ^{104}In

I^π_i	I^π_f	E_γ [keV]	b exp.	B(M1)[mW.u.] exp.	calc.
7^+_2	6^+_1	213	0.98(1)	350(20)	550
9^+_1	8^+_1	411	0.09(1)	> 7	837
9^+_1	8^+_2	204	0.20(2)	> 116	2.2
10^+_1	9^+_2	175	0.69(2)	110(10)	6.0
10^+_1	9^+_1	242	0.20(2)	12.3(12)	2.8
11^+_2	10^+_1	357	1	580(200)	230
12^+_1	11^+_1	816	0.35(2)	> 7	160
12^+_1	11^+_2	752	0.65(2)	> 20	375
10^-_1	9^-_1	524	0.75(1)	> 26	0.02
11^-_1	10^-_1	573	0.73(3)	> 20	13.8
12^-_1	11^-_1	458	0.78(4)	> 40	2.6
12^-_2	11^-_1	464	0.50(3)	280(70)	1.0
13^-_1	12^-_1	257	0.19(1)	> 70	1000
13^-_1	12^-_2	251	0.81(1)	> 300	2.7
14^-_1	13^-_1	286	1	1540(120)	920
15^-_1	14^-_1	540	1	> 200	742
				B(E2)[W.u.]	
9^+_1	7^+_1	1259	0.55(2)	> 0.8	2.4
9^+_1	7^+_2	1131	0.16(2)	> 0.4	4.3
10^+_1	8^+_1	653	0.11(2)	0.68(7)	0.13
11^-_1	9^-_1	1097	0.27(3)	> 1.0	7.9
12^-_1	10^-_1	1031	0.22(4)	> 1.0	0.001
12^-_2	10^-_1	-	n.o.	-	1.1
				B(E1) [W.u.] exp.	
(10^-_1)	(9^+_1)	1185	0.25(1)	$> 1.3 \cdot 10^{-5}$	
(12^-_1)	(11^+_2)	1615	0.18(4)	$> 3.7 \cdot 10^{-6}$	
(12^-_2)	(11^+_1)	1686	0.18(2)	$2.9(6) \cdot 10^{-5}$	
(12^-_2)	(11^+_2)	1621	0.09(2)	$1.6(5) \cdot 10^{-5}$	
(12^-_2)	(11^+_1)	1150	0.23(3)	$1.2(3) \cdot 10^{-4}$	
(13^-_1)	(12^+_2)	947	0.09(2)	$> 9.3 \cdot 10^{-6}$	

tion space to a maximum of one neutron in the $h_{11/2}$ shell and up to two neutrons in the $d_{3/2}$ orbit leads to good agreement between calculated and experimental excitation energies and most M1 and E2 transition probabilities. Calculations for ^{104}In using the same restrictions concerning the valence neutrons as in ^{105}In reproduce the level energies in this nucleus much better than previous calculations with a larger configuration space. On the other hand, these calculations do not account very well for the experimental transition probabilities in ^{104}In, especially for the predicted weak M1 transitions.

The results of this study show that for nuclei with N>50, shell model calculations considering all the orbits between the N=50 and N=82 shell closures but restricting the number of simultaneously excited neutrons, reach as good agreement with experiment as similar calculations of nuclei with N<50 discussed in a recent compilation by Rudolph et al. [20]. If, in addition, more lifetimes in the light Sn [21] and Cd isotopes become available, the door is opened for a comprehensive comparison of transition probabilities in nuclei on both sides of the N=50 line and to an improved understanding of the shell model structure in the ^{100}Sn region.

The authors appreciate very much the hospitality granted to them by INFN Legnaro and the excellent conditions for carrying out the experiment. This work has been supported by Deutsches Bundesministerium für Bildung, Wissenschaft, Forschung und Technologie (BMBF).

References

1. H. Grawe et al., Physica Scripta. **T56**, (1995) 71
2. A. Johnson et al., Nucl. Phys. **A557**, (1993) 401c
3. G. de Angelis et al., Nucl. Phys. **A 583**, (1995) 231c
4. M. De Poli et al., Physica Scripta. **T56**, (1995) 296
5. D. Seweryniak et al., Nucl. Phys.**A589**, (1995) 175
6. J. Kownacki et al., Nucl. Phys.**A627**, (1997) 239
7. S. Frauendorf and J. Reif, Nucl. Phys. **A621**, (1997) 738
8. R. Schubart et al., Z. Phys.**A352**, (1995) 373
9. M. Ishii et al., Physica Scripta **T56**, (1995) 89
10. T. Ishii et al., Z. Phys. **A343**, (1992) 261
11. A. Dewald et al., Nucl. Phys. **A545**, (1992) 822
12. GASP Collaboration Report, INFN/Be-90/11 (1990), C. Rossi-Alvarez, Nucl. Phys. News Europe **3** (1993) 10
13. D. B. Fossan and E. K.Warburton, in *Nuclear Spectroscopy and Reactions, Vol C* (Academic Press, New York 1974), K.P. Lieb, in D.N. Poenaru and W. Greiner (Edit.) *Experimental Techniques in Nuclear Physics* (Walter de Gruyter, Berlin 1997)
14. A. Dewald et al., Z. Phys. **A334**, (1989) 163
15. G. Böhm, A. Dewald, P.Petkov and P. von Brentano, Nucl. Instr. Meth. **A329**, (1993) 248
16. P. Lancaster and K. Salkauskas, *Curve and Surface Fitting*, (Academic Press, London 1986), C. Lingk et al., Phys. Rev. **C56**, (1997) R2349
17. P. Petkov et al., Nucl. Phys. **A543**, (1992) 589
18. D. Zwarts, Comput. Phys. Comm. **38**, (1985) 365
19. F. Rösel et al., At. Data Nucl. Data Tables **21**, (1978) 91
20. D. Rudolph, K.P. Lieb, H. Grawe, Nucl. Phys. **A597**, (1996) 298
21. M. Górska et al., Phys. Rev. **C58**, (1998) 108